Journal of Solid State Chemistry 229 (2015) 87–96

Contents lists available at ScienceDirect

Journal of Solid State Chemistry

journal homepage: www.elsevier.com/locate/jssc

Thermal expansion of mullite-type $Bi_2Al_4O_9$: A study by X-ray diffraction, vibrational spectroscopy and density functional theory

M. Mangir Murshed [a,*], Cecilia B. Mendive [b], Mariano Curti [b], Malik Šehović [a], Alexandra Friedrich [c], Michael Fischer [d], Thorsten M. Gesing [a]

[a] Chemische Kristallographie fester Stoffe, Institut für Anorganische Chemie, Universität Bremens, Leobener Straße, D-28359 Bremen, Germany
[b] Departamento de Química, Facultad de Ciencias Exactas y Naturales, Universidad Nacional de Mar del Plata, Dean Funes 3350, B7600AYL Mar del Plata, Argentina
[c] Institut für Geowissenschaften, Abteilung Kristallographie, Goethe-Universität Frankfurt, Altenhöferallee 1, D-60438 Frankfurt am Main, Germany
[d] Kristallographie, FB Geowissenschaften, Universität Bremen, Klagenfurter Straße, D-28359 Bremen, Germany

ARTICLE INFO

Article history:
Received 18 February 2015
Received in revised form
2 May 2015
Accepted 4 May 2015
Available online 21 May 2015

Keywords:
Mullite-type
Thermal expansion
Equation of state
Phonon
Density functional theory
Modeling

ABSTRACT

Polycrystalline $Bi_2Al_4O_9$ powder samples were synthesized using the glycerine method. Single crystals were produced from the powder product in a Bi_2O_3 melt. The lattice thermal expansion of the mullite-type compound was studied using X-ray diffraction, Raman spectroscopy and density functional theory (DFT). The metric parameters were modeled using Grüneisen approximation for the zero pressure equation of state, where the temperature-dependent vibrational internal energy was calculated from the Debye characteristic frequency. Both the first-order and second-order Grüneisen approximations were applied for modeling the volumetric expansion, and the second-order approach provided physically meaningful axial parameters. The phonon density of states as well as phonon dispersion guided to set the characteristic frequency for simulation. The experimental infrared and Raman phonon bands were compared with those calculate from the DFT calculations. Selective Raman modes were analyzed for the thermal anharmonic behaviors using simplified Klemens model. The respective mode Grüneisen parameters were calculated from the pressure-dependent Raman spectra.

1. Introduction

Mullite-type $Bi_2M_4O_9$ (M=Al^{3+}, Ga^{3+}, Fe^{3+}) and isotypic $Bi_2Mn_4O_{10}$ compounds have been drawn considerable interests due to their diverse crystal-chemical as well as physical properties ([1,2] and Refs. Therein). Whereas most of the solid oxide fuel cells function at high temperatures (> 1000 °C) the bismuth containing oxides can better serve at low temperatures. $Bi_2Al_4O_9$ has been shown to have an intrinsic conductivity of about 10^{-2} Ω/cm at 800 °C, which is largely, but not completely, ionic [3]. The high conductivity claimed for $Bi_{1.8}Sr_{0.2}Al_4O_{9-\delta}$ at high temperature (1073 K) [4] was explained in terms of impurities of Bi_2O_3 produced at elevated temperatures [5,6]. The weak Bi–O bond strength promotes a greater mobility of the vacancies in the Bi_2O_3 lattice (25% of the oxygen sites in the structure are unoccupied), however, makes the material more reducible in hydrogen. $Bi_2A1_4O_9$ was reported to show green photoluminescence at 300 K [7–9] whereas photoluminescence at room temperature is a rare phenomenon for bismuth containing compounds. Both the photoluminescence and relaxation data (25 ns) make the $Bi_2Al_4O_9$ crystals an attractive material for scintillation detectors, in particular for pulse high energy electron-beam registration. Fig. 1 shows the crystal structure of $Bi_2Al_4O_9$ characterized by the edge-sharing AlO_6 octahedra running parallel to the crystallographic **c**-axis. The AlO_6 octahedral chains are interconnected by two AlO_4 tetrahedra with a common oxygen vertex. The Bi^{3+} cation resides in the framework channels forming a nido-like trigonal bipyramidal BiO_4E coordination where the nido-position provides space for the stereoactive 6 s^2 lone electron pair (LEP, in formula abbreviated as E). Taking bismuth–oxygen long distances (~300 pm) into account Bi^{3+} locates at the centroid of a highly distorted BiO_6 octahedron. In some recent investigations we observed that the photocatalytic activity of $Bi_2Al_4O_9$ for degrading the methylene blue at natural pH appeared to be higher than that of $Bi_2(Al_{1-x}Fe_x)_4O_9$ with x=0.3, 0.6 or 0.9 [10]. While the catalysis and conductivity are observed at higher temperatures the knowledge of thermal behaviors of $Bi_2Al_4O_9$ is of crucial importance. Mullite and mullite-type materials are suitable candidates for ceramics [1]. Therefore, their thermophysical property in particular the thermal expansion is important for a wide variety of applications for cookwares, electronic devices, dental applications, zero-expansion heat sinks, engine components, spark plugs,

* Corresponding author. Tel.: +49 (0)421 218 63144; fax: +49 (0)421 218 63145.
E-mail address: murshed@uni-bremen.de (M. Mangir Murshed).

http://dx.doi.org/10.1016/j.jssc.2015.05.010
0022-4596/

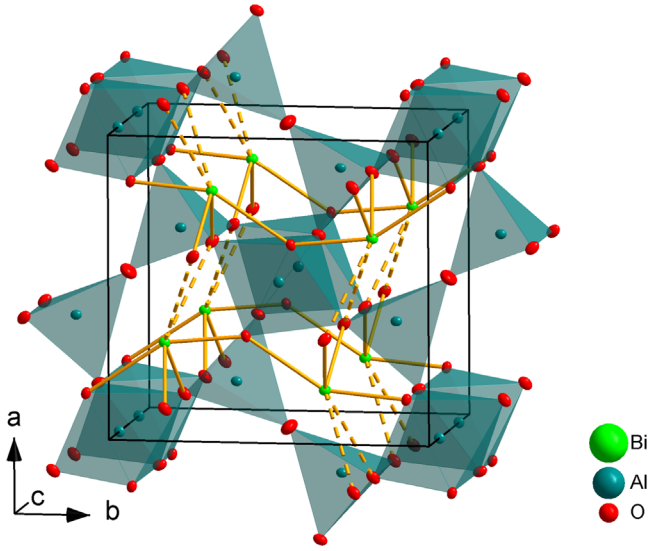

Fig. 1. Crystal structure of $Bi_2Al_4O_9$ showing the edge-sharing AlO_6 octahedra running parallel to the **c**-axis.

catalyst supports, high performance optical mirror substrates etc. Materials with anisotropic thermal expansion are useful against thermal shocks and micro-cracks in the ceramics. Moreover, anisotropic thermal expansion is a tool to subdue the volumetric expansion of some low symmetry materials; however, the underlying microscopic reasons are not well established. From this standpoint $Bi_2Al_2O_9$ can be considered as a model compound which possesses a low symmetry (orthorhombic) along with stereochemically active LEPs. Herein, we report the thermal expansion of $Bi_2Al_2O_9$ using X-ray diffraction, Fourier transform infrared (FTIR) and Raman spectroscopes, and density functional theory (DFT) calculations.

It is well established in many crystal systems that the LEP leads to either structural instabilities [11] or a strong steric effect resulting in structural stabilities. Due to the presence of the Bi^{3+} LEP, $Bi_2Al_4O_9$ is of the latter kind. Like other elements of group-15, the Bi^{3+} cation forms polar covalent bonds with oxygen sharing *p*-electrons, while its *s*-electron shell can easily be deformed by lattice vibrations, leading to strong anharmonicity. Consequently, the microscopic features for the thermal expansion of $Bi_2Al_4O_9$ may not be straightforward. Temperature-dependent Raman scattering would help to understand the anharmonicity of the phonons and their consequent physical effects on the solids, in particular, for the change of thermal expansion, specific heat and thermal conductivity. The anharmonic phonon is an effect of phonon-phonon interactions, which play key roles in thermal expansion and carrier transport properties of materials. The present study thus includes the modeling of some selective phonon frequencies and their line-widths with respect to temperature.

2. Experimental

2.1. Synthesis

Polycrystalline $Bi_2Al_4O_9$ powder samples were synthesized using the glycerine method [12] from a stoichiometric mixture of $Bi(NO_3)_3 \cdot 5H_2O$ and $Al(NO_3)_3 \cdot 9H_2O$ together with 10 wt% of glycerine. The mixtures were put into a glass beaker and first heated at 353 K under stirring as long as NO_x evolved, and finally at 473 K for two hours. The sample was then crushed into powder and homogenized, put into a platinum crucible and heated at 1210 K for 48 h. The crucible was then removed from the furnace for rapid cooling. The sample was then washed using diluted nitric acid to remove remaining Bi_2O_3. Single crystals were produced by heating the $Bi_2Al_4O_9$ powder product with an excess (four times in weight) of Bi_2O_3 at 1240 K for one day followed by cooling the melt at 2 K/h to 1210 K and held at this temperature for additional three hours. For large single crystals (mm- to cm-sized) the top seeded solution growth technique was used as described by Burianek et al. [13].

2.2. Single crystal X-ray diffraction

For single-crystal X-ray diffraction data collection, a crystal ($0.04 \times 0.05 \times 0.10$ mm^3) was selected, mounted on the top of a small glass fiber and fixed within a metal pin. Temperature-dependent single crystal X-ray diffraction was performed on a Bruker AXS D8 Venture equipped with a KAPPA four-circle goniometer. The PHOTON 100 detector based on CMOS technology provided an active area of 100 cm^2. The experiments were carried out using Mo*K*α ($\lambda = 71.073$ pm) radiation. A curved graphite crystal TRIUMPH served as monochromator. The attached Bruker KRYOFLEX II was used for nitrogen gas cold stream and temperature was controlled by the software suite. A semi-empirical approach was applied for absorption correction for equivalent reflections, leading to a $R_{int} \sim 0.06$ with a fluctuation of ± 0.01 for different temperature dataset. During the refinement with anisotropic displacement parameters for all atoms a total of 44 parameters were varied resulting in final residuals of $R_1 = 0.024$ for $969 F_O > 4\ \sigma\ F_O$ and 0.036 for all 1166 data. The refined atomic coordinates, anisotropic and equivalent isotropic displacement obtained from the room temperature data are given in Table 1. The obtained crystallographic features are in excellent agreement with the corresponding reported values [14]. For the bismuth atoms four bonds to oxygen atoms were observed at 213.0(2) pm (2 × O2), 214.5(3)upm (O11) and 240.4(3)mpm (O11). For the octahedrally coordinated Al1 position the Al1–O distances were found as 186.5(2)es wer × O12), 192.9(2)epm (2 × O11) and 194.4 (2) pm (2 × O12). The Al_2O_4 tetrahedral coordination shows Al2–O bond lengths of 173.7(1) pm (O3), 175.5(3)mpm (O12) and 172.3(2) mpm (2 × O2). Taking the respective bond valence parameters [15] the BiO_4, $Al1O_6$ and $Al1O_4$ polyhedra, respectively show bond valence sum of 3.10(1) a.u., 2.97(1) a.u. and 2.91(1) a.u., proving the global instability index of 0.192(1) a.u.

2.3. Powder X-ray diffraction

X-ray diffraction measurements were carried out for the synthesized powder products followed by structure refinements with the fundamental parameter approach using the "Diffrac^{Plus} Topas 4.2" (Bruker AXS GmbH, Karlsruhe) software. High-temperature data were collected on a PANalytical MPD powder diffractometer in Bragg–Brentano geometry equipped with a secondary Ni filter, Cu*K*α radiation and a X'Celerator multi-strip detector using an Anton Paar HTK1200N heating chamber. The sample was prepared in a flat corundum sample holder with a small evaporation channel that served as additional space for thermal expansion. Measurements were carried out between 300 K and 990 K with step of 10 K. Each pattern was recorded from 10° to 100° 2θ with a step size of 0.0167° and a scan time of 200 s/step. For the Rietveld refinement the starting atomic coordinates were taken from the room-temperature single crystal X-ray data (Table 1). The composite data obtained from single crystal (100–300 K) and powder (300–990 K) X-ray diffraction experiments were used to study the lattice thermal expansion of $Bi_2Al_4O_9$.

2.4. Spectroscopy

The temperature-dependent Raman spectra were collected on a pressed pellet produced from the powder sample. The spectra were recorded on a LabRam ARAMIS (Horiba Jobin Yvon) micro-Raman spectrometer equipped with a laser working at 785 nm and less than 20 mW. The use of a 50 × long working distance objective (Olympus) with a numerical aperture of 0.55 provides a focus spot of about 2 μm diameter when closing the confocal hole to 200 μm. Raman spectra were collected in the range 80 cm^{-1} to 1200 cm^{-1} with a spectral resolution of approximately 1.2 cm^{-1} using a grating of 1800 grooves/mm and a thermoelectrically-cooled CCD detector (Synapse, 1024 × 256 pixel). The spectral position and the linearity of the spectrometer were calibrated against the Raman mode (520.7 ± 0.1 cm^{-1}) of a Si wafer and the emission lines of a neon lamp, respectively. For the low-temperature measurements, the pellet was placed on a Linkam cooling stage (THMS600) attached to a pump (LNP95 Cooling Pump) that provides a continuous flow of liquid nitrogen. Measurements of the high-temperature spectra were performed placing the sample in a Linkam heating stage (TS1500). A heating rate of 5 K/min and a holding time of 10 min prior to the data collection were followed for better equilibration for both low- and high-temperature measurements within a fluctuation of ±0.1 K at each measuring temperature.

The pressure-dependent micro-Raman spectra were performed using a Renishaw Raman spectrometer (RM-1000) equipped with a HeNe laser (532 nm, 200 mW). A 20 × long working distance objective was used. A single crystal (ca. 40 mm × 30 mm × 10 mm) was pressurized in a Boehler–Almax diamond-anvil cell with neon as the pressure medium.

Each spectrum was baseline corrected and fitted (Pseudo-Voigt) with the 'LAMP' software [16]. The Pseudo-Voigt line-shape is a convolution of the natural Lorentzian line-shape of the Raman phonon with the instrumental Gaussian broadening. The instrumental broadening was checked using different slit configurations and measured for the $\lambda = 585.249$ nm emission line of a neon lamp, which was fitted with a Gaussian line-shape providing the line-width Γ_G of 1.88 cm^{-1}. Then the intrinsic phonon line-widths were calculated using the Voigt profile approximation: $\Gamma_V \approx 0.5346\Gamma + (0.2166\Gamma^2 + \Gamma_G^2)^{0.5}$, where Γ_V and Γ refer to the observed and Lorentzian intrinsic phonon line-width, respectively.

The FTIR spectrum was recorded on a Bruker IFS 66v/S using both KBr (mid-infrared) and ethylene pellet (far-infrared) using 2 mg and 1 mg samples, respectively. Both spectra were adjusted and summed into a single spectrum.

2.5. DFT

Periodic calculations were performed with the crystalline orbital program CRYSTAL09 [17,18], employing the PW1PW hybrid Hartree Fock—Density Functional Theory (HF—DFT) method [19]. The structure of $Bi_2Al_4O_9$ was optimized starting from the low temperature single crystal data. The basis sets were taken from the CRYSTAL website database [20]. A very large integration grid with 75 radial points and 974 angular points was adopted. The Monkhorst–Pack shrinking factor was set to 4 after checking energy convergence of the structures, that is, 27 independent *k*-points in the irreducible Brillouin zone were taken. Geometry optimizations were done under a hydrostatic constant pressure as implemented in CRYSTAL09 [18]. By changing the pressure to the desired value, the different pressure-dependent unit-cell volumes were obtained. The constant pressure constrained geometry optimizations were performed at 0, 5, 10, 15, 20 and 25 GPa as given in Table 2. The 3rd-oder Birch–Murnaghan isothermal EoS was used to calculate the zero-pressure volume (V_0), isothermal bulk modulus (K_0) and pressure derivative of K_0 (K_0').

$$P(V) = \frac{3}{2}K_0\left[\left(\frac{V_0}{V}\right)^{7/3} - \left(\frac{V_0}{V}\right)^{5/3}\right]\left\{1 + \frac{3}{4}(K_0' - 4)\left[\left(\frac{V_0}{V}\right)^{2/3} - 1\right]\right\} \quad (1)$$

The EoS parameters were also calculated from the internal energy $E(V)$ term expressed by the integration of pressure $P(V)$:

$$E(V) = E_0 + \frac{9V_0K_0}{16}\left\{K_0'\left[\left(\frac{V_0}{V}\right)^{2/3} - 1\right]^3 + \left[\left(\frac{V_0}{V}\right)^{2/3} - 1\right]^2\left[6 - 4\left(\frac{V_0}{V}\right)^{2/3}\right]\right\} \quad (2)$$

The fittings of these two approaches are shown in Fig. 2. The obtained V_0, K_0 and K_0' are in good agreement with the

Table 1
Atomic coordinates, anisotropic and equivalent isotropic displacement parameters of $Bi_2Al_4O_9$ obtained from single crystal X-ray diffraction data at ambient condition.

Pbam: $a = 771.77(3)$ pm, $b = 810.68(4)$ pm, $c = 569.28(3)$ pm. $R_{obs} = 0.024$, $R_{all} = 0.036$

Atom	Wyckoff	Site sym.	Occupancy	*x*	*y*	*z*
Bi	4g	..*m*	1	0.32929(2)	0.16737(2)	0
Al1	4e	..2	1	0	0	0.26078(20)
Al2	4h	..*m*	1	0.14895(17)	0.33937(15)	1/2
O11	4g	..*m*	1	0.35807(41)	0.43054(36)	0
O12	4h	..*m*	1	0.36308(41)	0.41215(37)	1/2
O2	8i	1	1	0.12813(29)	0.20633(24)	0.25001(41)
O3	4d	..2/*m*	1	0	1/2	1/2

Anisotropic displacement parameters × 10^4/pm^2

Atom	U_{11}	U_{22}	U_{33}	U_{12}	U_{13}	U_{23}	U_{eq}
Bi	0.0040(1)	0.0035(1)	0.0051(1)	−0.0002(1)	0	0	0.0042(1)
Al1	0.0045(5)	0.0039(4)	0.0027(5)	0.0004(4)	0	0	0.0037(2)
Al2	0.0026(5)	0.0032(5)	0.0033(6)	−0.0000(4)	0	0	0.0031(2)
O11	0.0067(12)	0.0005(11)	0.0053(14)	−0.0003(9)	0	0	0.0042(5)
O12	0.0051(12)	0.0055(12)	0.0029(13)	−0.0009(10)	0	0	0.0045(5)
O2	0.0076(8)	0.0049(7)	0.0036(10)	−0.0008(7)	−0.0013(8)	−0.0008(8)	0.0054(4)
O3	0.0082(18)	0.0069(17)	0.0207(23)	0.0034(17)	0	0	0.0119(8)

Table 2
Pressure-dependent metric parameters from DFT, their bulk moduli and first derivatives of the bulk moduli with respect to pressure in comparison to the experimental values.

DFT (CRYSTAL09) calculated metric parameters				
P (GPa)	a (pm)	b (pm)	c (pm)	V (pm^3 $\times 10^6$)
0	769.37	809.49	570.28	355.17
5	757.51	801.42	564.14	342.48
10	746.93	794.78	558.83	331.75
15	737.41	789.49	554.19	322.64
20	728.54	785.09	550.15	314.67
25	719.59	781.64	546.76	307.53
Fit parameters using Eqs. (1) and (2) for cell volume (V_0), bulk modulus (K_0) and the pressure derivative (K'_0) of K_0				
EoS para.	[a]DFT	[b]DFT	Fit-1	Fit-2
V_0 (pm^3 $\times 10^6$)	355.17	355.17	356.93(9)	356.7
K_0 (GPa)	126.4	126.72	122(2)	126.3
K_0'	4.4	4.86	4.9(3)	4.45

[a] Pressure-dependent data.
[b] Energy-dependent data. Fit-1 and Fit-2 refer to fitting performed on the experimental data [29] by the corresponding ref. and present work, respectively.

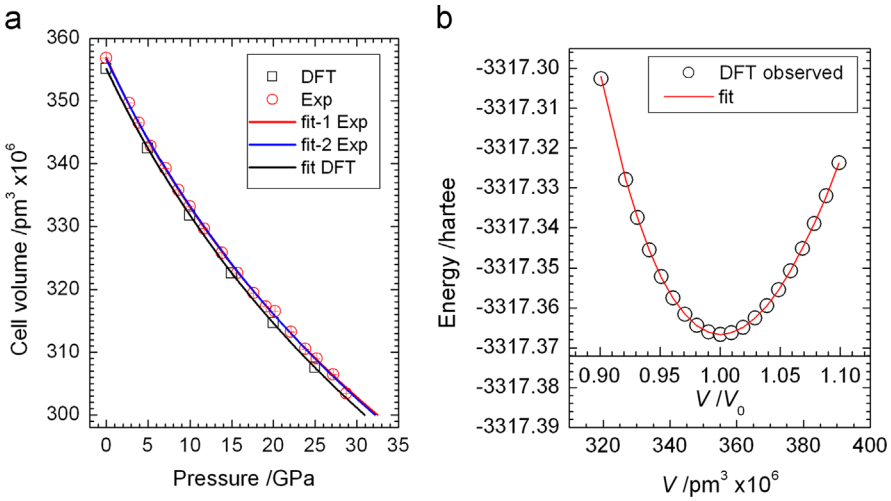

Fig. 2. (a) Pressure-dependent volume change of $Bi_2Al_4O_9$ together with the 3rd-order Birch–Murnaghan EoS fit. Fit-1 and fit-2 refer to the 3rd-order Birch-Murnaghan EoS fitted by Ref. [29] and this study. (b) Optimization of cell volume varying the lattice parameter and fitting the energy from the integration of pressure.

experimental values (Table 2). Harmonic frequencies at the Γ-point of the Brillouin zone at 0 K were calculated by computing numerically the second derivatives of the energy with respect to the atomic positions, and diagonalizing the mass-weighted Hessian matrix in Cartesian coordinates as implemented in CRYSTAL09 [18,21]. The calculated IR and Raman modes were identified changing the atomic mass in different calculations.

The phonon density of states (PDOS) and the phonon mode dispersions were calculated using the plane-wave DFT code CASTEP [22]. An energy cut-off of 830 eV was used, and norm-conserving pseudo-potentials were employed to describe the core electrons. A $2 \times 2 \times 3$ mesh of k-points was used to sample the Brillouin zone. The calculations used the PBEsol exchange-correlation functional, which was developed specifically for solids [23]. To calculate the vibrational properties, the vibrational density-functional perturbation theory formalism was employed [24]. A $3 \times 3 \times 4$ Monkhorst–Pack mesh of q-vectors was used in the dynamical matrix calculations. The PDOS and the partial contribution of each atom in the asymmetric unit were plotted using a smearing of 0.1 THz (3.34 cm^{-1}). Each PDOS spectrum was normalized in a way that the integral of DOS equals to one.

3. Results and discussion

3.1. X-ray diffraction and thermal expansion

The metric parameters obtained from single crystal and powder X-ray diffractions at ambient conditions are in excellent agreement, that is, the low-temperature data successively follow the high-temperature ones with almost identical value at some given temperatures close to 300 ($\pm$10) K. Thermal expansion discrepancy due to single crystal and the polycrystalline powder was not encountered, and the composite data serve to follow the thermal expansion. The expansion behaviors of the metric parameters are shown in Fig. 3; almost similar behaviors of the corresponding ones in $Bi_2Ga_4O_9$ [25]. For a comparison, the axial bulk moduli for $Bi_2Ga_4O_9$ (K_a=230.4(4)GPa, K_b=309.5(5) and K_c=446(2)GPa, in the crystallographic a- b- and c-direction) and $Bi_2Fe_4O_9$ (K_a=163.6(1)GPa, K_b=303.8(5)GPa and K_c=431.6(1)GPa) were calculated [26] from the observed elastic constants [27,28]. López-de-la-Torre et al. [29] observed the similar trend for $Bi_2Al_4O_9$ and $Bi_2Mn_4O_{10}$ compounds, showing that the linear incompressibities of these isotypic materials follow the order as $K_c > K_b > K_a$. However, the axial thermal expansion coefficient

(α_a, α_b and a_c, respectively for *a*-, *b*- and *c*-cell parameter) follows as $\alpha_b > \alpha_c > \alpha_a$ at ambient condition. Alike mullite, the thermal expansion behavior violates the empirical rule (the lowest thermal expansion occurs to the elastically stiffest crystal direction). This discrepancy was explained in terms of pure geometric considerations [27–29], however, the underlying microscopic reason is still unclear. The phonon density of states (PDOS) and its partial components from each atom in the asymmetric unit (Bi, Al, O) are shown in Fig. 4. The calculated phonon dispersion of its equilibrium structure along some high-symmetry points are also depicted (Fig. 4a). The negligible negative frequency of the acoustic modes in the Γ-point is associated with the numerical error in calculation. The acoustic phonons show usual dispersion with no avoided crossing of significance in the first Brillouin zone. Most of the optical branches are dispersionless (flattened). The spreading of the phonons demonstrates the continuum of the PDOS up to 680 cm^{-1} (Fig. 4b). An isolated continuum between 680 cm^{-1} and 850 cm^{-1} is also noticeable. Moreover, two well

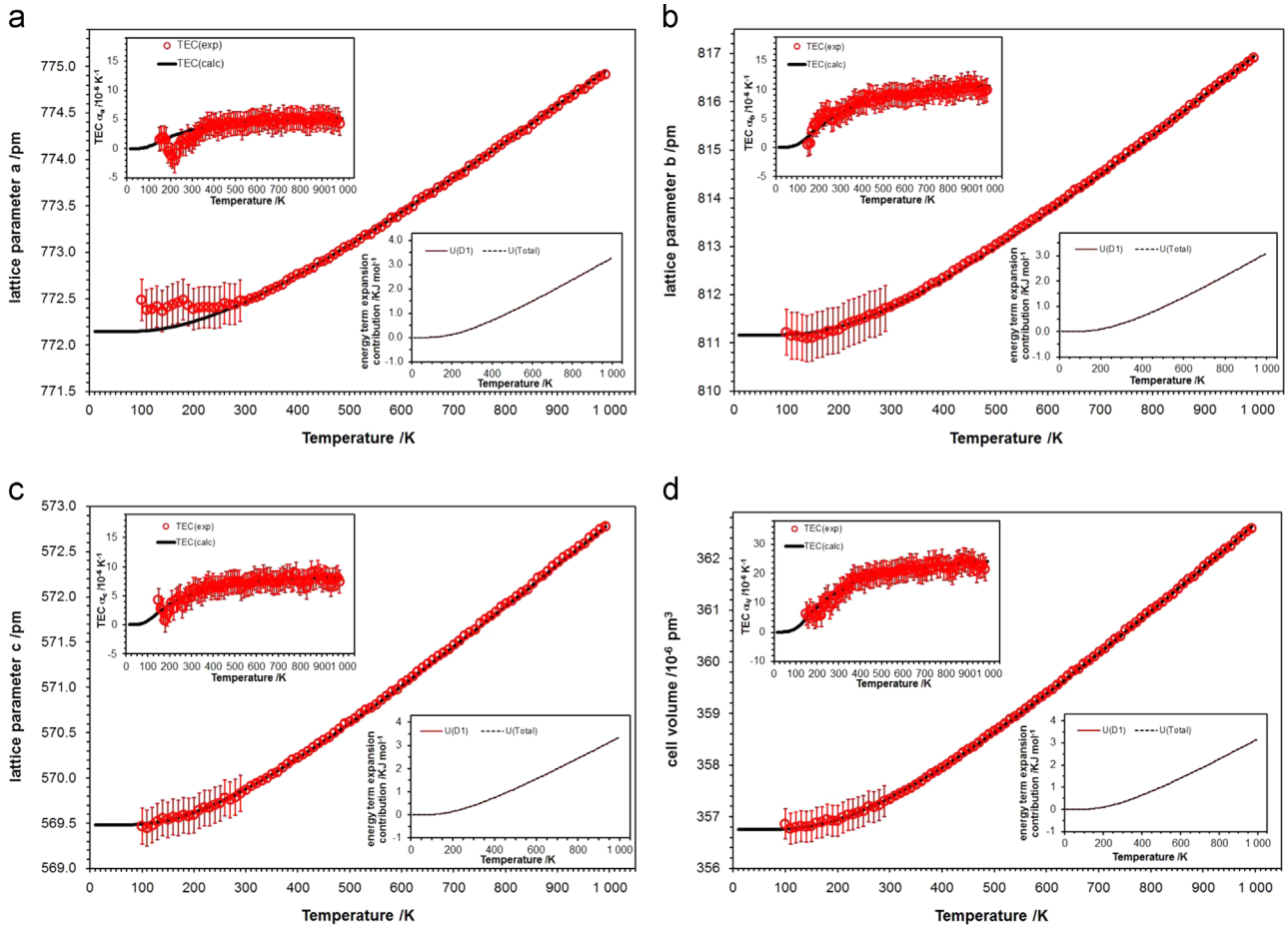

Fig. 3. Thermal expansion of the metric parameters together with the respective model (solid line). Temperature-dependent thermal expansion coefficients of the corresponding cell parameters and the energy calculation are given insets. (a) *a*-cell parameter, (b) *b*-cell parameter, (c) *c*-cell parameter and (d) cell volume.

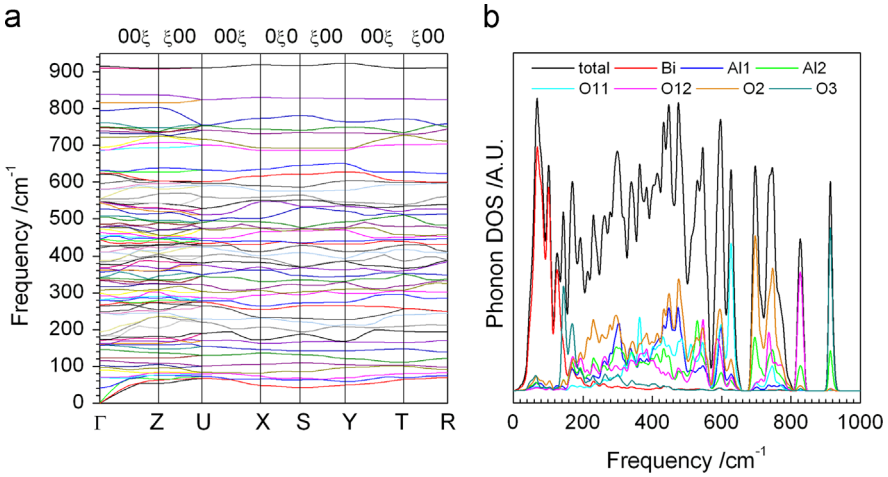

Fig. 4. (a) Phonon dispersion of $Bi_2Al_4O_9$ in some high symmetry directions. (b) Phonon density of states (PDOS) of $Bi_2Al_4O_9$.

separated high frequency dispersionless optical modes can be seen, showing a phonon band gap between 850 cm^{-1} and 920 cm^{-1}. From these considerations the whole PDOS continuum can be explained in terms of two Debye spectra along with a single Einstein-type frequency. In the PDOS the lower-frequency (<200 cm^{-1}) region is exclusively contributed by bismuth. The mid-range is equally contribute by aluminum and oxygen, and the higher-frequency region is dominated by lighter oxygen atoms. The possible Einstein-type frequency seems to be mainly contributed by O3 with the eigenvector normal to the Al2-O3 bond as supported by the thermal ellipsoid (Table 1). The electronic band gap of $Bi_2Al_4O_9$ is about 4.3(1) eV as calculated by means of CRYSTAL09 at 0 K and 0 GPa [10], categorizes this compound as a wide band gap semiconductor. The set point of the ionic conductivity was reported to occur at 1073 K [3]. Therefore, the thermal expansion excludes any electronic as well as ionic contribution, and can be explained purely from the lattice vibrational internal energy. In some recent reports we modeled the thermal expansion of mullite-type materials [25,30] using Grüneisen first-order approximation for the zero-pressure EoS as follows:

$$V(T) = V_0 + \frac{\gamma U(T)}{K_0} \tag{3}$$

where K_0 and γ are isothermal bulk modulus and thermodynamic Grüneisen parameter, respectively. It is well known that calculation of $U(T)$ for polyatomic solids such as $Bi_2Al_4O_9$ is difficult using Debye quasi-harmonic model. Because the parabolic Debye phonon spectrum with a characteristic cut-off frequency cannot explain the Van Hove singularities in the PDOS. Accordingly, for a better description we described the $U(T)$ as an additive term of harmonic, quasi-harmonic and anharmonic contributions to model the thermal expansion of isotypic $Bi_2Ga_4O_9$ [25] and mullite-type $PbFeBO_4$ [30] using the following expression:

$$V(T) = V_0 + \sum_{i=1}^{d} k_{Di} U_{Di}(T) + \sum_{j=1}^{e} k_{Ej} U_{Ej}(T) + k_A U_A(T) \tag{4}$$

where k_{Di}, k_{Ej} and k_A are adjustable fitting parameters contributing to Debye (U_{Di}), Einstein (U_{Ej}) and anharmonic (U_A) energies, respectively. In this regard the PDOS can guide to set characteristic frequencies to model the cell volume expansion. For instance, as a first approximation the PDOS of $Bi_2Al_4O_9$ can be explained as a combination of two independent Debye cut-offs and one Einstein type characteristic frequencies for the first (0–680 cm^{-1}) and the second (680–850 cm^{-1}) continua, and the dispersionless high frequency narrow band at 920 cm^{-1}, respectively. However, the simulation converges to only a single Debye term ($i=1$) with characteristic temperature of 1090 (11) K (758(8) cm^{-1}) where

$$U(T) = 9Nk_BT\left(\frac{T}{\theta_D}\right)^3 \int_0^{\frac{\theta_D}{T}} \frac{x^3}{\exp(x)-1} dx \tag{5}$$

N refers to the number of atoms per unit cell ($N=30$) and k_B is the Boltzmann constant. A slight contribution from the anharmonicity term at higher temperature was neglected. Notably, the V_0 contains the zero-point energy $9Nk_B\theta_D/8$ for the Debye term, and the integral term of the Debye function is evaluated numerically. The obtained k_D ($7.52(1)\times10^{-12}$ Pa^{-1}) evaluates $\gamma=0.95(1)$ using K_0 of 126.3 GPa as given in Table 3. The obtained Debye frequency 758 (8) cm^{-1}) falls at the middle of the second continuum of the PDOS (Fig. 4b). Fig. 3a shows the excellent fit between the model and the observed cell volume. Using Eq. (4) it is possible to model the axial thermal expansion, however, with no physically meaningful parameters. Extending the first-order Grüneisen approximation to second order can help in this regard. That is, the Taylor expansion

Table 3
Fitting parameters of the temperature-dependent metric parameters of $Bi_2Al_4O_9$ using first-order Grüneisen (FOG) and second-order Grüneisen (SOG) approximations.

Model	Metric	θ_D (K)	γ	M_0	K_0 (GPa)	K_0'
FOG	V_0 ($pm^3.10^6$)	1090(11)	0.95(1)	356.75(5)	126.3	–
SOG	V_0 ($pm^3.10^6$)	1046(12)	0.91(1)	356.75(5)	126.3	4.9
SOG	a_0 (pm)	1379(52)	0.56(1)	772.32(1)	324	12
SOG	b_0 (pm)	930(21)	1.06(1)	811.10(1)	360	16
SOG	c_0 (pm)	873(21)	1.06(1)	569.45(5)	444	14.7

Thermodynamic bulk moduli K_0, K_{0a}, K_{0b}, K_{0c} of the metric parameters and their respective pressure derivatives K'_0, K'_{0a}, K'_{0b}, K'_{0c} are taken from [29]. Each axial bulk modulus and their respective pressure-derivatives were multiplied with a factor of 3 according to [34]

of PV to higher-order ΔV leads to the following expression [31]:

$$V(T) = V_0 + \left[\frac{U(T)}{Q - BU(T) + C^2\{U(T)\} + \cdots}\right] \tag{6}$$

The denominator converges rapidly at higher orders, where $Q=V_0K_0/\gamma$, $B=1/2(K'_0-1)$ and C are adjustable parameters, and K'_0 is the derivative of K_0 with respect to pressure. Restricting the perturbation up to second order as used by Vocadlo et al. [32] and Lindsay-Scott et al. [33] Eq. (6) turns into be:

$$V(T) = V_0 + V_0\left\{\frac{U(T)}{\frac{V_0K_0}{\gamma} - \frac{U(T)}{2}(K'_0-1)}\right\} \tag{7}$$

Using axial bulk modulus such as K_{a0} and its pressure-derivative K'_{a0} Eq. (7) can also be used to model the thermal expansion of a cell parameter (also similar for b- and c-cell parameters), and allow extracting axial Grüneisen parameter (γ_a) and Debye temperature (θ_a) from the following expression:

$$a(T) = a_0 + a_0\left[\frac{U_a(T)}{\frac{V_0K_{a0}}{\gamma_a} - \frac{U_a(T)}{2}\left\{K'_{a0} - \frac{2K_{a0}}{K_{b0}} - \frac{2K_{a0}}{K_{c0}} - 1\right\}}\right] \tag{8}$$

Considering axial bulk modulus for an orthorhombic system Eq. (8) is the modified version of Eq. (7) where the axial bulk modulus and the respective pressure-derivative values (Table 3) are taken into account. Of relevant notes, the axial bulk modulus and the axial pressure-derivatives of an orthorhombic system are in general three times greater than their volumetric equivalent [34], because, $K_0=1/(1/3K_{a0}+1/3K_{b0},+1/3K_{c0})$ and $K'_0=1/(1/3K'_{a0}+1/3K'_{b0},+1/3K'_{c0})$. For the fitting of the cell parameters we used the experimentally obtained constants. López-de-la-Torre et al. [29] extracted the axial bulk moduli from the normalized pressure vs Eulerian strain plots, and hinted for corresponding pressure-derivatives ($K'_{a0}\sim4$, $K'_{b0}>4$ and $K'_{c0}>4$) based on the degree of inclination of the model line. We take slightly different values (Table 3) for the pressure-derivatives as the model straight line for b-cell parameter is sharper than that of c (Ref. [29], Fig. 10, top panel). The applied model provides an excellent description of the behavior of the individual cell parameters as well as the cell volume over the full temperature range. The reason for appearance of a slight negative thermal expansion in the a-direction below 200 K may due to the known fact that the expansivity of the single crystal can slightly vary from its polycrystalline counterpart. The mean value of both the Debye temperature (1061(35) K) and the Grüneisen parameter (0.89(1)) calculated from the corresponding axial values are in good agreement with the respective volumetric fit (Table 3).

3.2. Spectroscopy

Factor group analysis predicts 90 vibrational modes ($12A_g+9A_u+12B_{1g}+9B_{1u}+9B_{2g}+15B_{2u}+9B_{3g}+15B_{3u}$) with three acoustic modes ($B_{1u}+B_{2u}+B_{3u}$), 36 infrared active modes ($8B_{1u}+14B_{2u}+14B_{3u}$), 42 Raman active modes ($12A_g+12B_{1g}+9B_{2g}+9B_{3g}$) and nine ($A_u$) silent modes (neither infrared nor Raman active in first order). Fig. 5 shows the infrared and Raman spectra along with the fitted and calculated band positions. The experimentally observed infrared and Raman phonon frequencies are compared in Tables 4 and 5, respectively, with those calculated by CRYSTAL09 and CASTEP. The discrepancy either in frequency value or mode assignment calculated by CRYSTAL09 and CASTEP can be understood within the scope of the associated parameters. For instance, the eigenvectors and the associated vibrational energy in the mid-range of the PDOS of the system are intrinsically complicated, which additionally harbors discrepancy in particular for mode assignments. Fitting the whole range IR spectrum at ambient condition required 28 bands between 80 cm^{-1} and 1000 cm^{-1}. The obtained band maxima are in good agreement with the reported ones in the MIR regions [35]. The low temperature (78 K) Raman spectrum required 31 bands (Fig. 5b), most of which (extrapolated down to 0 K) well agree with those calculated by DFT. The pressure-dependent Raman spectra are shown in Fig. 6. The pressure derivatives ($\partial\omega_i/(P)$ were used to calculate the mode-Grüneisen parameters, $\gamma_i=K_0(1/\omega_{i0})(\partial\omega_i/\partial P)$ and ω_{i0}=mode frequency at zero pressure (Table 5). Since the calculated and the experimental bulk moduli are close to each other, the disagreements of some γ_i values mainly stem from the range of pressure encountered (exp. up to 25 GPa and CRYSTAL09 up to 10 GPa) and the nonlinear behavior of some modes. For instance, modes below 150 cm^{-1} are associated with BiO_6 octahedra, showing at least two different slopes (0–7 GPa and 7–25 GPa). The temperature-dependent Raman shift of most frequencies exhibit normal behavior as usual in ionic crystals, that is, frequency decreases and line-width increases with increasing temperature. For anharmonic analyses some representative phonons ω_i were chosen for i=106, 121, 273 and 324 (corresponding to the Raman shift in cm^{-1} at 0 K). The selection was made for phonons which are well separated at any given temperature. Anharmonicity of the phonon modes involve phenomena beyond those of the independent phonons. The higher-order phonon–phonon interactions are the main source of the anharmonic behavior, which causes the frequency of the harmonic oscillators in a crystalline solid to be temperature dependent. The temperature dependency of the phonon frequency arises from two different sources: (i) a pure-volume effect associated with the thermal expansion, and (ii) a pure-temperature effect that is present even at a constant volume. To reveal the temperature-dependent Raman mode behavior we follow the modified Klemens model [36]. The temperature-dependent frequency of a Raman phonon mode can be written according to the following expression:

$$\omega_i(T)=\omega_{i0}+\Delta\omega_i(T) \quad (9)$$

$\Delta\omega_i(T)$ refers to total shift, which is an additive term of two

Table 4
Calculated and experimental IR phonon frequencies of $Bi_2Al_4O_9$.

ω_{CRYS09}	ω_{CASTEP}	ω_{Exp}	I_{CRYS09}	I_{CASTEP}	I_{Exp}	M_{CRYS09}	M_{CASTEP}
94.29	90.14	96.58	3.25	1.33	11.64	B3u	B2u
120.70	122.13	–	0.05	0.04	0.00	B2u	B3u
141.04	157.38	–	17.86	0.01	0.00	B1u	B1u
159.15	159.56	159.19	10.41	6.15	21.84	B3u	B2u
160.04	162.11	165.91	1.23	9.08	10.66	B1u	B3u
163.19	170.34	172.44	11.15	2.54	0.00	B2u	B1u
175.64	174.16	–	8.88	3.99	31.86	B3u	B2u
195.33	182.99	184.64	6.86	3.41	27.78	B2u	B3u
249.15	245.99	204.12	1.12	0.24	20.00	B2u	B3u
295.44	279.37	251.20	2.35	0.60	3.60	B3u	B2u
295.95	280.78	285.56	0.26	0.00	1.51	B2u	B3u
299.16	291.21	288.66	3.20	0.62	4.36	B1u	B1u
313.49	307.25	296.98	0.27	0.45	13.39	B3u	B2u
347.76	340.50	353.28	20.71	13.20	44.05	B3u	B2u
373.00	355.81	372.88	46.23	27.89	24.29	B2u	B3u
401.44	382.46	377.67	9.24	7.36	19.45	B2u	B3u
409.93	387.85	398.67	5.75	0.28	38.18	B3u	B2u
429.44	411.38	421.42	10.05	0.26	11.10	B1u	B1u
469.37	445.12	470.21	11.51	4.47	32.31	B3u	B2u
475.30	453.07	–	0.70	0.02	0.00	B1u	B1u
482.64	463.98	–	0.47	4.69	0.00	B2u	B3u
496.91	476.93	–	82.55	30.28	0.00	B3u	B2u
501.69	485.74	496.76	100.00	32.50	72.43	B1u	B3u
516.99	543.74	521.79	60.24	55.54	29.44	B2u	B2u
534.07	547.27	–	45.42	5.14	0.00	B3u	B3u
577.60	548.84	535.74	7.75	13.66	100.00	B2u	B1u
616.14	580.32	571.85	4.93	11.01	67.42	B1u	B1u
641.03	624.68	600.88	0.93	3.65	27.34	B2u	B2u
678.19	632.26	649.38	1.58	0.77	10.64	B3u	B3u
709.51	721.90	691.23	73.71	11.59	45.20	B1u	B2u
740.16	734.30	728.06	22.57	26.71	85.79	B3u	B3u
767.25	739.25	771.61	0.18	1.39	79.67	B2u	B2u
777.53	747.62	–	51.39	4.00	0.00	B2u	B3u
781.90	794.43	845.53	0.78	100.00	14.61	B3u	B1u
958.36	910.27	920.23	19.13	11.94	68.08	B3u	B2u
965.04	915.45	943.11	10.92	7.80	17.72	B2u	B3u

ω, M and I refer to frequency (cm^{-1}), mode (Irre. Rep.) and normalized intensity (A. U.), respectively. The subscript refers to associated method.

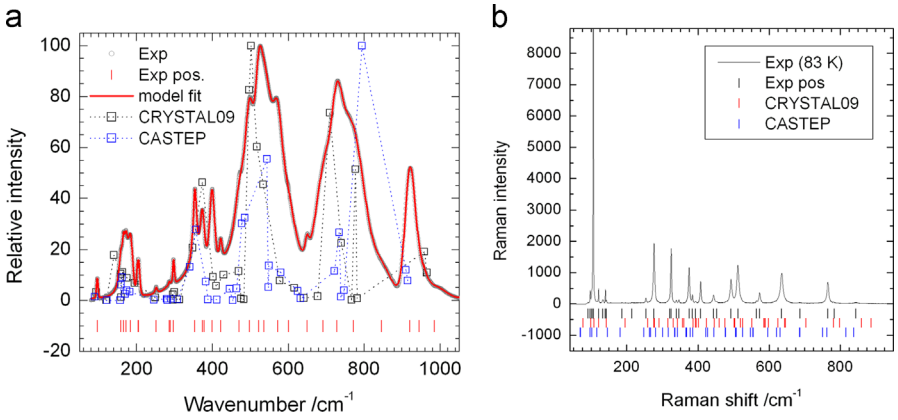

Fig. 5. (a) Raman spectrum of $Bi_2Al_4O_9$ together with fitted and DFT calculated (0 K) band frequency. (b) Infrared spectrum of $Bi_2Al_4O_9$ at ambient condition together with fitted and DFT calculated (0 K) band frequency and intensity.

Table 5
Calculated and experimental Raman phonon frequencies of $Bi_2Al_4O_9$ together with their corresponding mode Grüneisen parameters.

ω CRYS09 at 0 K	ωCASTEP at 0 K	ωExp at 78 K	ωPD at 298 K	γPD	γCRYS09	MCRYS09	MCASTEP
77.11	68.68	–	–	–	−1.0(2)	B2g	B2g
77.48	70.20	–	–	–	−0.08(2)	B3g	B3g
99.00	96.92	97.2(1)	–	–	0.25(2)	Ag	Ag
108.1	102.38	105.5(1)	103.1(3)	1.98 (5)	1.82(2)	Ag	Ag
120.76	115.65	120.7(1)	119.9(3)	0.91 (9)	0.77(4)	B1g	B1g
143.27	146.18	140.1(1)	138.3(1)	1.00 (3)	0.93(3)	B1g	B1g
195.47	181.93	186.9(1)	184.1(1)	0.7 (2)	−0.22(3)	B2g	B3g
258.42	247.96	253.3(2)	251.3(1)	0.57 (8)	0.48(2)	B3g	B2g
275.42	263.59	274.1(2)	273.8(1)	-0.20 (1)	−0.10(3)	B1g	Ag
277.23	266.64	276.6(1)	280.7(4)	1.34 (8)	−0.14(4)	Ag	B1g
290.62	280.20	280.7(1)	–	–	0.15(1)	B3g	B2g
315.49	300.03	321.8(1)	311.5(6)	1.3(2)	0.06(2)	B2g	B3g
330.06	315.80	323.9(1)	322.2(3)	0.58 (4)	0.54(6)	Ag	Ag
342.47	334.09	338.9(1)	–	–	0.19(2)	B1g	B2g
356.07	335.09	345.9(2)	344.6(6)	0.53 (4)	0.43(6)	B3g	B1g
360.45	341.93	369.9(1)	–	–	0.52(8)	B2g	B3g
386.55	366.33	374.9(1)	373.3(1)	0.38 (2)	0.24(1)	Ag	B3g
393.14	368.09	383.9(1)	385.0(3)	0.83 (4)	0.78(1)	B3g	B2g
394.81	377.64	394.4(1)	–	–	0.74(1)	B2g	Ag
401.17	385.43	407.7(1)	405.5(7)	0.92 (2)	0.55(2)	B1g	B1g
424.02	421.63	–			0.87(4)	Ag	B3g
445.86	427.02	443.3(1)	441.4(4)	0.68 (3)	0.31(2)	B2g	B2g
460.19	444.42	–	–	–	0.57(3)	B3g	B3g
475.25	444.99	–	477.6(9)	1.66 (6)	1.33(6)	B2g	B1g
501.46	476.68	492.4(1)	490.5(6)	0.37 (1)	0.35(1)	Ag	B2g
503.49	477.42	–	–	–	1.44(3)	B3g	Ag
519.87	505.38	511.7(1)	509.2(5)	0.68 (3)	0.62(1)	Ag	B1g
525.21	508.02	–	–	–	0.70(6)	B1g	Ag
551.09	526.06	–	–	–	0.55(1)	B1g	B1g
584.96	547.14	565.9(1)	–	–	0.35(1)	B1g	B1g
586.59	547.54	573.6(1)	571.4(8)	0.52 (2)	0.47(1)	Ag	B2g
589.41	554.07	–	–	–	0.77(3)	B3g	Ag
598.16	555.07	–	–	–	1.00(2)	B2g	B3g
625.13	596.28	–	614.9(5)	0.25 (3)	0.62(2)	B1g	B1g
644.28	621.51	635.6(1)	632.6(1)	0.73 (2)	0.73(3)	Ag	Ag
645.66	631.51	–	–	–	0.64(2)	B1g	B1g
703.36	685.61	686.4(1)	–	–	1.03(3)	B2g	B2g
703.83	687.19	–	690.6(9)	1.08 (3)	1.04(3)	B3g	B3g
781.65	751.05	765.1(1)	762.8(1)	–	0.70(2)	Ag	Ag
798.12	762.34	782.8(1)	–	0.75 (2)	0.67(2)	B1g	B1g
860.25	816.37	843.4(1)	840.2(4)	0.83 (3)	0.78(4)	Ag	Ag
887.54	838.69	869.3(1)	–	–	0.74(4)	B1g	B1g

ω, γ, and M refer to frequency (cm^{-1}), mode Grüneisen parameter and mode (Irr. rep.). The subscript refers to associated method (PD=pressure-dependent experimental data).

contributions as follows:

$$\Delta\omega_i(T) = \Delta\omega_i^{latt}(T) + \Delta\omega_i^{anh}(T) \quad (10)$$

$\Delta\omega_i^{anh}(T)$ refers to the frequency shift due to phonon–phonon interactions; the term is also known as the pure temperature contribution. $\Delta\omega_i^{latt}(T)$ is the frequency shift due to volume thermal expansion. Assuming that both K_0 and γ_i are temperature independent, the term $\Delta\omega_i^{latt}(T)$ can be expressed as:

$$\Delta\omega_i^{latt}(T) = \omega_{i0}\left[\exp\left\{-\int_0^T \gamma_i\alpha_V(T)dT\right\} - 1\right] \quad (11)$$

The observed $\Delta\omega_i^{anh}(T)$ can be modeled considering the phonon decay into two channels namely, 3-phonon and 4-phonon interactions [36]:

$$\Delta\omega_i^{anh}(T) = A\left[1 + \frac{2}{\exp\left(\frac{hc\omega_{i0}}{2k_BT}\right) - 1}\right] + B\left[1 + \frac{3}{\exp\left(\frac{hc\omega_{i0}}{3k_BT}\right) - 1} + \frac{3}{\left\{\exp\left(\frac{hc\omega_{i0}}{3k_BT}\right) - 1\right\}^2}\right] \quad (12)$$

A and B are damping factors given in Table 6, representing the relative probability of the occurrences of the 3-phonon (cubic decay) and 4-phonon (quartic decay) processes contributing to the frequency shift, respectively. The model well describes our observed data for the anharmonic phonon contribution to the frequency shift as shown in Fig. 7. All modes smoothly soften, and $\Delta\omega_i^{anh}(T)$ mostly dominates over $\Delta\omega_i^{latt}(T)$ for the whole temperature range. However, mode ω_{106} showed an opposite behavior at low temperature, which may due to strong steric effect of LEP on the volume of the BiO_6 octahedron. In general, the observed spectral data appearing elsewhere above and below the model line demonstrate hardening and softening of the corresponding mode, respectively. A slight drop down of the anharmonicity in particular for high frequency modes above 1000 K is noticeable. Since 1073 K is the set point of the ionic conductivity [3], it may be associated with the ionic mobility of Bi-atoms. The low frequency modes require lower damping factors than those of high frequency modes (Table 6), indicating that the lighter elements oxygen and aluminum mostly contribute to the thermal anharmonicity to the crystal. The high frequency ω_{844} mode assigned to Al2–O stretching, which hardly follows the applied model (symmetric decay). Since this broad feature of the mode may be a combination of Al2–O and Al1–O stretching, the compound nature of the mode may not follow the model. The intrinsic line-width of a Raman phonon mode in a defect-free sample mainly comes from two

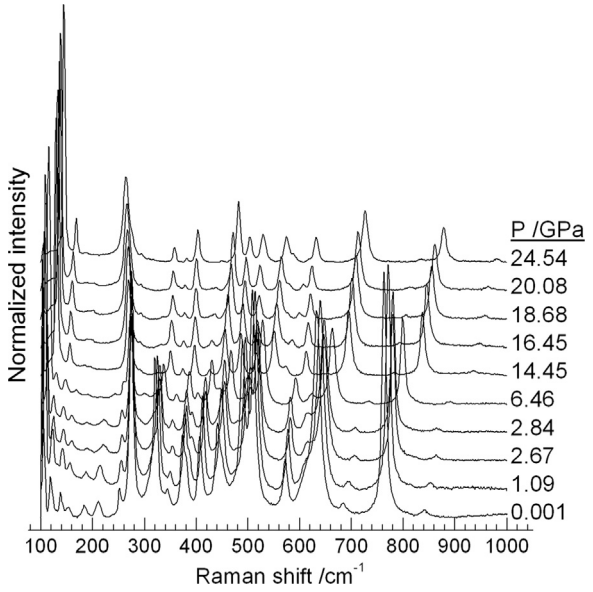

Fig. 6. Pressure-dependent Raman spectra collected on a single crystal of $Bi_2Al_4O_9$ at room temperature.

Table 6
Selective Raman frequencies at 0 K, their corresponding mode Grüneisen parameters together with the fitting parameters used for Eqs. (12) and (13).

ω_{i0} (cm^{-1})	$(\gamma_i)_T$	A (cm^{-1})	B (cm^{-1})	Γ_0 (cm^{-1})	C (cm^{-1})	D (cm^{-1})
97.5	0.25(2)	−0.108(5)	−0.0010(3)	1.73(2)	0.044(2)	–
105.7	1.98(5)	−0.091(1)	–	0.466(4)	0.047(5)	0.0004(1)
120.8	0.91(9)	−0.054(2)	−0.0005(1)	1.78(3)	0.041(5)	0.0005(1)
140.1	1.00(3)	−0.124(5)	−0.0006(1)	0.25(5)	0.187(4)	–
276.5	1.34(8)	−0.432(2)	−0.0180(1)	1.18(8)	1.81(1)	–
324.0	0.58(4)	−1.501(2)	−0.1055(1)	2.28(3)	1.69(4)	–
407.7	0.92(2)	−0.75(7)	−0.0077(6)	4.08(5)	1.362(1)	0.0862(1)
492.5	0.37(1)	−1.932(2)	–	3.02(6)	2.80(1)	0.3013(2)
512.0	0.68(3)	−3.413(2)	−0.2405(2)	2.84(4)	5.97(1)	–
635.8	0.73(2)	−3.313(1)	–	3.82(10)	8.659(3)	–
765.7	0.75(2)	−4.603(3)	–	3.31(8)	6.565(12)	0.0762(2)
843.4	0.83(3)	–	−0.5370(5)	5.88(20)	11.99(5)	–

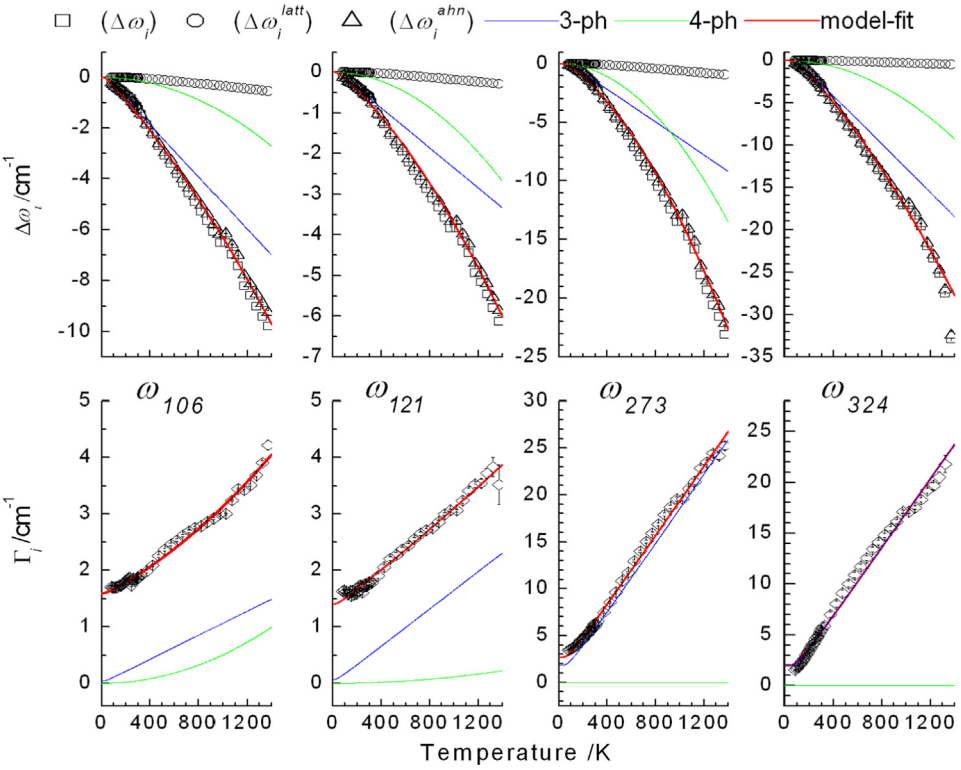

Fig. 7. Temperature-dependent change of phonon frequencies (top) linewidth (bottom) of some representative Raman bands of $Bi_2Al_4O_9$. The triangle (Δ), circle (○) and square (q) refer to frequency shift due to volume contribution ($\Delta\omega_i^{latt}$), anharmonic contributions ($\Delta\omega_i^{anh}$) and observed line-width (Γ_i), respectively. The solid lines represent model calculations based on phonon–phonon interactions.

terms: (i) electron–phonon and (ii) phonon–phonon interactions. The electron–phonon interaction usually appears at very low temperatures and was not considered to analyze the temperature-dependent mode broadening (Fig. 7). The temperature-dependent line-widths of the modes have been modeled using the Balkanski approach [37], however, with an extended form as applied in some recent works ([38] and Ref. therein):

$$\Gamma_i(T) = \Gamma_{i0} + C\left[1 + \frac{2}{\exp\left(\frac{hc\omega_{i0}}{2k_BT}\right) - 1}\right] + D\left[1 + \frac{3}{\exp\left(\frac{hc\omega_{i0}}{3k_BT}\right) - 1} + \frac{3}{\left\{\exp\left(\frac{hc\omega_{i0}}{3k_BT}\right) - 1\right\}^2}\right] \quad (13)$$

Γ_{i0} refers to a contribution from the inherent defect or impurity scatterings at 0 K. The second and third term correspond to symmetric decay of 3-phonon and 4-phonon channels with anharmonic constants C and D, respectively. Fig. 7 (bottom) shows the temperature-dependent change of the line-widths along with the model lines for different contributions. The substantial contributions of both the 3-phonon and 4-phonon processes to frequency broadening of the modes are also given (Table 6). Thermal emission particularly hampers and limits the line-width analyses due to mode disappearance, overlapping and increasing background. The theoretical model well fits most of the observed data. A smooth non-linear change of the line-width at low temperature followed by a high-temperature linear steep rise explains the usual symmetric decay of the observed modes.

4. Conclusion

The modeling of the lattice thermal expansion of mullite-type $Bi_2Al_4O_9$ is a continuation of our recent works [25,30,39] with an improved microscopic modeling strategy. The CRYSTAL09 and

CASTEP based DFT calculations assign the IR and Raman vibrational modes of $Bi_2Al_4O_9$ together with a comparison between experimental observations and theoretical approaches. The Debye characteristic frequency (758(8) cm^{-1}) required to fit the volume thermal expansion of $Bi_2Al_4O_9$ did not cover the high frequency region of the PDOS. However, the axial Debye temperature (958 (36) cm^{-1}) in the *a*-direction lies close to the highest frequency (943 cm^{-1}) observed in the FTIR spectrum. This discrepancy lies within the limitation of the Debye elastic approximation. In a Debye solid the constituent atoms contribute a constant proportion of the total PDOS at each frequency. But it is clear from the PDOS that the atomic contributions tend to localize in certain regions of the spectrum. For instance, Bi dominates to the low-frequency part, while light oxygen and aluminum to the high-frequency region. Amid such limitation the change of the vibrational energy calculated from a single Debye frequency used in the second-order Grüneisen approximation well fit the thermal expansion of the metric parameters.

Acknowledgments

We gratefully acknowledge the Deutsche Forschungsgemeinschaft (DFG) for the financial support through the mullite-LEP project GE1981/4-1. TMG especially acknowledges the DFG for a support in the Heisenberg program (GE1981/3-1). MF would like to thank Dr. Rolf Arvidson and Prof. Andreas Lüttge (Marum) for generous access to the Asgard cluster. MF acknowledges funding by the Central Research Development Fund (CRDF) of the University of Bremen (Funding line 04 - Independent Projects for Post-Docs). AF acknowledges financial support from the DFG within priority program SPP1236 (FR2491/2-1).

References

[1] H. Schneider, Mechanical properties of mullites, in: H. Schneider, S. Komarneni (Eds.), Mullite, Wiley-VCH, Weinheim, 2005, pp. 141–164.
[2] R.X. Fischer, H. Schneider, The mullite-type family of crystal structures, in: H. Schneider, S. Komarneni (Eds.), Mullite, Wiley-VCH, Weinheim, 2005, pp. 1–46.
[3] I. Bloom, M.C. Hash, J.P. Zebrowski, K.M. Myles, M. Krumpelt, Solid State Ionics 53-56 (1992) 739.
[4] S. Zha, J. Cheng, Y. Liu, X. Liu, G. Meng, Solid State Ionics 156 (2003) 197.
[5] Th.M. Gesing, M. Schowalter, C. Weidenthaler, M.M. Murshed, G. Nénert, C. B. Mendive, M. Curti, A. Rosenauer, J.-Ch. Buhl, H. Schneider, R.X. Fischer, J. Mater. Chem. 22 (2012) 18814.
[6] S. Ohmann, P. Fielitz, L. Dörrer, G. Borchardt, Th.M. Gesing, R.X. Fischer, C. H. Rüscher, J.-C. Buhl, K.-D. Becker, H. Schneider, Solid State Ionics 211 (2012) 46.
[7] L.H. Brixner, Mater. Res. Bull. 13 (1978) 563.
[8] G. Blasse, O.B. Ho, J, Luminescence 21 (1980) 165.
[9] V.V. Volkov, A.V. Egorysheva, Opt. Mater. 5 (1996) 273.
[10] M. Curti, L. Granone, Th.M. Gesing, M.M. Murshed, T. Bredow, C.B. Mendive. International Center for Computational Materials Science-Workshop Functional Oxides for Emerging Technologies, Bremen, Germany, October-2013.
[11] A. Walsh, D.J. Payne, R.G. Egdell, G.W. Watson, Chem. Soc. Rev. 40 (2011) 4455.
[12] Th.M. Gesing, R.X. Fischer, M. Burianek, M. Mühlberg, T. Debnath, C.H. Rüscher, J. Ottinger, J.C. Buhl, H. Schneider, J. Eur. Ceram. Soc. 31 (2011) 3055.
[13] M. Burianek, M. Mühlberg, M. Woll, M. Schmücker, Th.M. Gesing, H. Schneider., Cryst. Res. Technol. 44 (2009) 1156.
[14] I. Abrahams, A.J. Bush, G.E. Hawkes, T. Nunes, J. Solid State Chem. 147 (1999) 631.
[15] N.E. Bresse, M. O'keeffe, Acta Crystallogr. B47 (1991) 192.
[16] D. Richard, M. Ferrand, G.J. Kearley, J. Neutron Res. 4 (1996) 33.
[17] R. Dovesi, R. Orlando, B. Civalleri, C. Roetti, V.R. Saunders, C.M. Zicovich-Wilson, Z. Kristallogr. 220 (2005) 571.
[18] R. Dovesi, V.R. Saunders, C. Roetti, R. Orlando, C.M. Zicovich-Wilson, F. Pascale, B. Civalleri, K. Doll, N.M. Harrison, I.J. Bush, P. D'Arco, M. Llunell, CRYSTAL09, CRYSTAL09 User's Manual, University of Torino, Torino, 2009.
[19] T. Bredow, A.R. Gerson, Phys. Rev. B 61 (2000) 5194.
[20] ⟨http://www.crystal.unito.it/Basis_Sets⟩.
[21] F. Pascale, C.M. Zicovich-Wilson, F. Lopez, B. Civalleri, R. Orlando, R. Dovesi, J. Comput. Chem. 25 (2004) 888.
[22] S.J. Clark, M.D. Segall, C.J. Pickard, P.J. Hasnip, M.I.J. Probert, K. Refson, M. C. Payne, Z. Kristallogr. 220 (2005) 567.
[23] J. Perdew, A. Ruzsinszky, G. Csonka, O. Vydrov, G. Scuseria, L. Constantin, X. Zhou, K. Burke, Phys. Rev. Lett. 100 (2008) 136.
[24] K. Refson, P.R. Tulip, S.J. Clark, Phys. Rev. B 73 (2006) 155114.
[25] M.M. Murshed, Th.M. Gesing., Mater. Res. Bull. 48 (2013) 3284.
[26] P. Ravindran, L. Fast, P.A. Korzhavyi, B. Johansson, J. Appl. Phys. 84 (1998) 4891.
[27] J. Schreuer, M. Burianek, M. Mühlberg, B. Winkler, D.J. Wilson, H. Schneider, J. Phys.: Condens. Matter 18 (2006) 10977.
[28] T.F. Krenzel, J. Schreuer, Th.M. Gesing, M. Burianek, M Mühlberg, H. Schneider, Int. J. Mater. Res. 103 (2012) 438.
[29] L. López-de-la-Torre, A. Friedrich, E.A. Juarez-Arellano, B. Winkler, D.J. Wilson, L. Bayarjargal, M. Hanfland, M. Burianek, M. Mühlberg, H. Schneider, J. Solid State Chem. 182 (2009) 767.
[30] M.M. Murshed, C.B. Mendive, M. Curti, G. Nénert, P.E. Kalita, K. Lipinska, A. L. Cornelius, A. Huq, Th.M. Gesing, Mater. Res. Bull. 59 (2014) 170.
[31] D.C. Wallace, Thermodynamics of Crystals, Dover, New York, NY, 1998.
[32] L. Vocadlo, K.S. Knight, G.D. Price, I.G. Wood, Phys. Chem. Miner. 29 (2002) 132.
[33] A. Lindsay-Scott, I.G. Wood, D.P. Dobson, Phys. Earth Planet. Inter. 162 (2007) 140.
[34] R.J. Angel, Rev. Mineral. Geochem. 41 (2000) 35.
[35] D. Voll, A. Beran, H. Schneider, Phys. Chem. Miner. 33 (2006) 623.
[36] P.G. Klemens, Phys. Rev. 148 (1966) 845.
[37] M. Balkanski, R.F. Wallis, E. Haro, Phys. Rev. B 28 (1983) 1928.
[38] T. Lan, X. Tang, B. Fultz, Phys. Rev. B 85 (2012) 094305.
[39] Th.M. Gesing, C.B. Mendive, M. Curti, D. Hansmann, G. Nénert, P- E. Kalita, K. E. Linpinska, A.L. Cornelius, M.M. Murshed, Z. Kristallogr. 228 (2013) 532.